University of Padua

Measurements of Molecular Crowding in Living Cells

SUPERVISOR

Professor Filippo Romanato

University of Padua, Dept. of Physics and Astronomy

CO-SUPERVISORS

Professor Marco Dal Maschio

University of Padua, Dept. of Biomedical Sciences

Professor Gian Michele Ratto

NEST, Scuola Normale Superiore, Pisa

CANDIDATE

Andrea Marchetti

STUDENT ID

1193561

Abstract

The intracellular environment is formed by a variegated and heterogeneous mixture of solutes, including free ions and larger molecules. These are characterised by relatively low diffusion coefficients and, in some extreme cases, get bound because of the interaction with large complexes of the cell like the cytoskeleton or other organelle structures. It is known that molecular crowding within the cell changes depending on local protein synthesis and degradation and that these changes induce ion fluxes (typically K^+, Na^+ and Cl^-) compensating for variation in osmolarity. Ions, in turn, play a role in the control of neuronal membrane potential and – therefore – in brain excitability.

Recent data suggest that in cortical neurons there is a strong daily fluctuation in Cl^- concentration. Given the connection between molecular crowding and ion fluxes, it is expected that molecular crowding can have an impact on these Cl^- fluctuations and, eventually, on the brain excitability itself. Following this hypothesis, the aim of this project is to design and validate a method based on Fluorescence Correlation Spectroscopy (FCS) and Raster Image Correlation Spectroscopy (RICS) to measure molecular crowding *in vitro* and to evaluate its extension to *in vivo* studies.

Contents

List of figures

1

Introduction

This thesis is based on a two-month long visiting activity at Scuola Normale Superiore of Pisa, where I joined Prof. Ratto's neuroscience group. The work was also carried out with the kind help of Prof. Francesco Cardarelli, who made available for us some instrumentation and instructed us on it.

1.1 MOTIVATIONS

Several studies on the physiology of the brain have pointed out a connection between diseases such as epilepsy or autism and anomalous values of chloride intracellular concentration [1]. Hence, a better understanding on the mechanisms involved in intracellular chloride regulation in the brain could lead to a better understanding of the mechanisms of epilepsy and autism, and could in the future lead to be able to correct the errors in regulation by means of pharmacological tools, aiming to reduce symptoms or even to control the diseases.

Work from Prof. Ratto's laboratory [2] suggests that the intracellular chloride concentration in pyramidal neurons of mice varies during the day following a circadian rhythm (figure 1.1, panel A).

Furthermore, in a recent paper Stangherlin et al. [3] identified and characterised the daily oscillations of soluble proteins and of the main ions (K^+, Ca^+, Cl^-) in the cytosol, finding that they follow a synchronised circadian rhythm of ≈ 24 h (figure 1.1, panel B). In particular, they observed that ion oscillations are antiphasic with respect to protein oscillations, proposing that ion fluxes buffer intracellular osmotic potential against daily variations in cytosolic soluble protein abundance, thus guaranteeing the total cellular volume remain constant. The amount of soluble proteins in the cytosol – i.e. proteins that are not sequestrated by the nucleus, organelles or membrane-less organelles – determines in turn molecular crowding, which influences the movement freedom of cytosolic proteins (figure 1.1, panel C).

Since Cl^- plays a role in controlling brain inhibition, molecular crowding and Cl^- circadian rhythm may play a role in the physiology of electrically active cells such as neurons. Hence, the final aim of the research will be to look for correlations between oscillations of chloride and proteins in *in vivo* neurons, a first step towards understanding the mechanisms of chloride regulation in the brain. The idea is therefore to measure molecular crowding at different moments of the day by means of non-invasive methods, providing a picture of the amount of cytosolic proteins present at every moment while maintaining the cells intact.
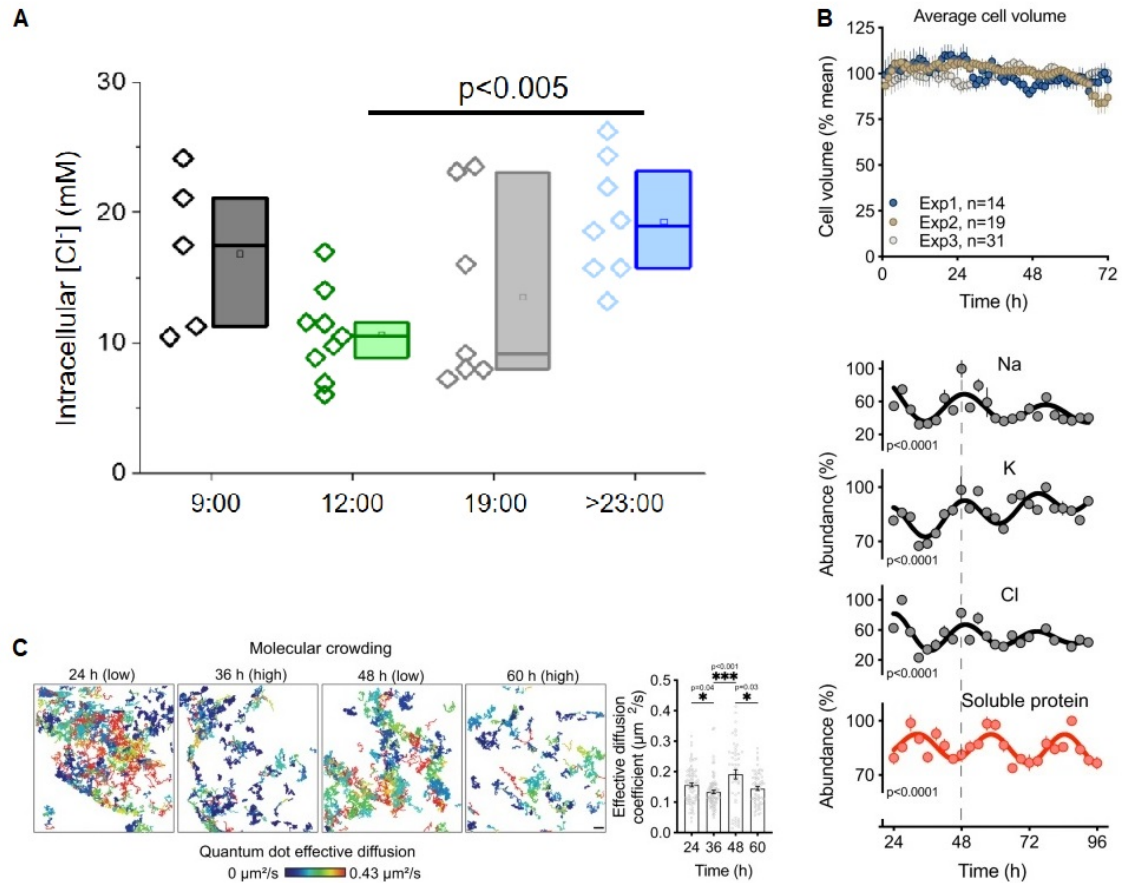
Figure 1.1: A picture of cellular circadian rhythm. (A) Diurnal intracellular oscillations of chloride concentration in *in vivo* murine pyramidal neurons: comparison of Cl^- amount at different moments of the day, with significant difference between 12:00 and 24:00 [2]. (B) Antiphasic synchronisation of soluble proteins and ions in *in vitro* fibroblasts, while average cell volume remains constant. Abundance values were normalised for the maximal value in each timeseries [3]. (C) Molecular crowding visualised by means of Single Particle Tracking (SPT) of quantum dots and associated diffusion coefficients: when soluble protein concentration is higher, quantum dots are less free to move and the diffusion coefficient is lower; when it is lower, quantum dots are more free to move and the diffusion coefficient is higher [3].

In this preliminary project we aimed at measuring molecular crowding *in vitro*, attempting to develop and validate a method to do it in view of adapting and applying it to the study of the circadian rhythm of molecular crowding in neurons, both in *in vitro* and in *in vivo* studies.

1.2 HOW TO MEASURE MOLECULAR CROWDING?

The eukaryotic cell's cytoplasm is composed by subcellular structures – like the nucleus, organelles, membrane-less organelles and the cytoskeleton – and by the cytosol, which is rich in proteins, ions and other molecules. Macromolecules make the cytoplasm a significantly viscous fluid if compared to water, with a relative viscosity η_{cyto}/η_{H_2O} of about 3 [4]. Actually, macromolecules may occupy 5 to 40 % of the total cellular volume [5], and their concentration values are typically in the range of 200-400 g/l [6, 7].

2
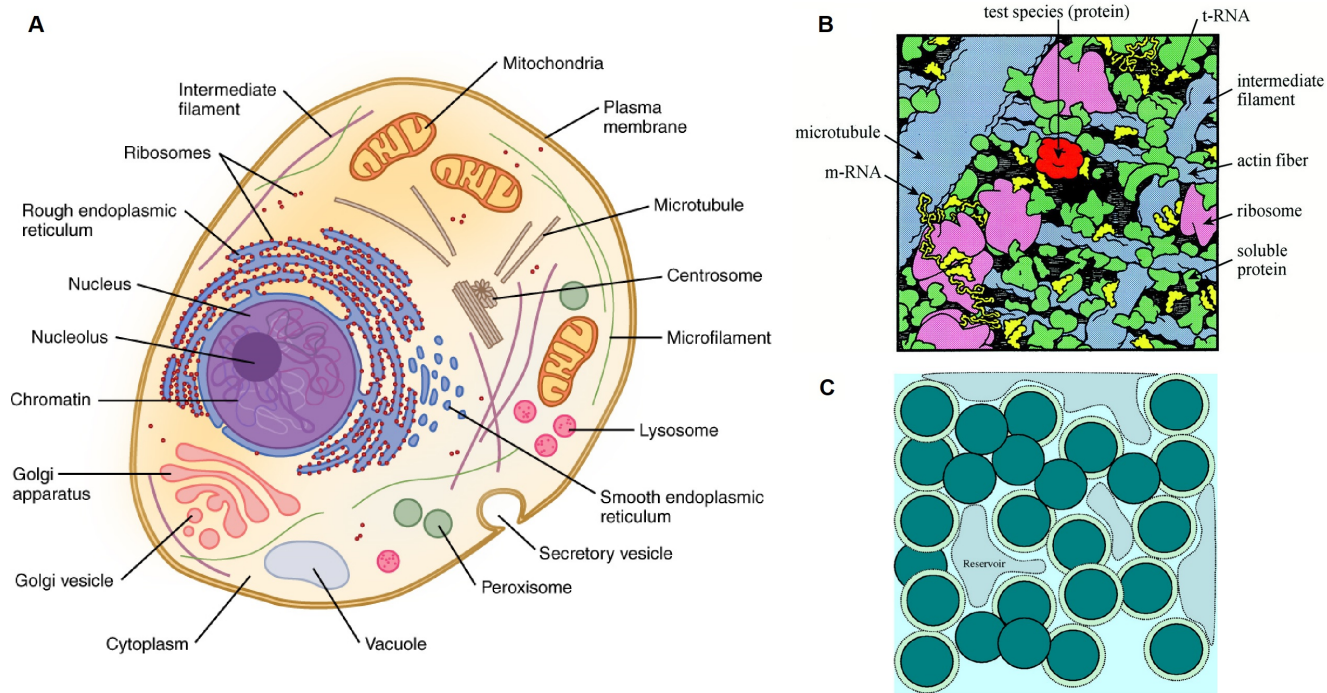
Figure 1.2: The eukaryotic intracellular environment. (A) Cartoon illustration of the eukaryotic cell with its main subcellular structures [8]. (B) Cartoon illustration of the crowdedness of the cytoplasm, at magnification of 1,000,000 times, with proteins, filaments, RNA and other structures gathering around the cytoskeleton [9]. (C) 2D cartoon representing the organisation of cytosol into macromolecular multiplexes and bulk water nanopools and reservoirs. Circles represent (uniformly) charged 5 nm macromolecules (dark green) stabilised by an aqueous Debye length of 0.7 nm (light green), corresponding to the typical ionic strength of the cytoplasm. In this model, spheres occupy 25% of the total volume [10].

The main way for macromolecules to move in the cell is diffusion. From an atomistic point of view, molecules follow a Brownian motion (first described by Robert Brown in 1827), wandering in the cytoplasm along a certain direction, until they hit another body; after the collision their direction will change, and in crowded environments the process will repeat many times. In presence of many molecules, the whole of single-molecule Brownian motions manifests at the macroscopic level as diffusion. The connection between the microscopic and the macroscopic levels is given by the following relation:

$$\langle x^2 \rangle = 2Dt \tag{1.1}$$

where $\langle x^2 \rangle$ is the 1D mean square displacement (i.e. the deviation of a particle position from its initial starting point, u.m. μm^2), D is the diffusion coefficient (u.m. $\mu m^2/s$) and t is time.
The diffusion coefficient is then amongst the main and most reliable descriptors of the diffusion phenomenon.
Diffusion of macromolecules in the cytosol is sensitive to several factors, particularly macromolecular crowding i.e., as macromolecule concentration increases, the diffusion of macromolecules decreases [11]. Indeed, the more crowded the environment, the higher the number of collisions for every molecule in the unit of time, the smaller the mean square displacement and the smaller the diffusion coefficient. By measuring diffusivity, we can therefore get information on molecular crowding.

A common technique to measure the diffusion coefficient in the cell consists in inserting fluorophores – i.e. molecules which emit light upon photon absorption – into the cell and analysing the radiation emitted by them. This allows to maintain the cell intact and alive and, therefore, hopefully as close as

possible to its natural configuration.

One of the most utilised fluorophores for this kind of measurements is Green Fluorescent Protein (GFP), a 27 kDa protein which emits mostly in the green wavelengths range. Free GFP in the cytoplasm has typical diffusion coefficient values of a few tens of $\mu m^2/s$ [12, 13, 14, 15, 16, 17, 18].

The fluorescent emission is collected by means of a microscope equipped with one or more detectors, which, together with the rest of the acquisition electronics, convert the photon signal into an electronic signal. This data can be subsequently analysed by means of several techniques, some of the most common of which are Fluorescence Correlation Spectroscopy (FCS) and Raster Image Correlation Spectroscopy (RICS). These belong to the category of fluctuation spectroscopy techniques, that process the intensity signal of the collected light by analysing the spontaneous fluorescence fluctuations at thermodynamic equilibrium, and can eventually return the diffusion coefficient of the fluorophores in the sample.

In further work, by performing several measurements at different times of the day, we may follow the oscillations of diffusion coefficient and so assess the presence of a circadian rhythm in molecular crowding.

1.3 THEORETICAL BACKGROUND

1.3.1 FLUOROPHORES

When an electron leaps from the ground state to an excited state after photon absorption, the excess energy can be released following many paths, through both radiative and non-radiative processes.

Radiative processes include fluorescence and phosphorescence; in particular, fluorescence consists in the relaxation of the electron back to the ground state with the emission of a photon, without any change in the original electron spin.

In non-radiative processes, on the other hand, the relaxation mechanisms do not involve the emission of light, competing with fluorescence emission and decreasing its efficiency. Examples include vibrational relaxation, internal conversion, intersystem crossing to the triplet state and energy transfer to another molecule (e.g. quenching).
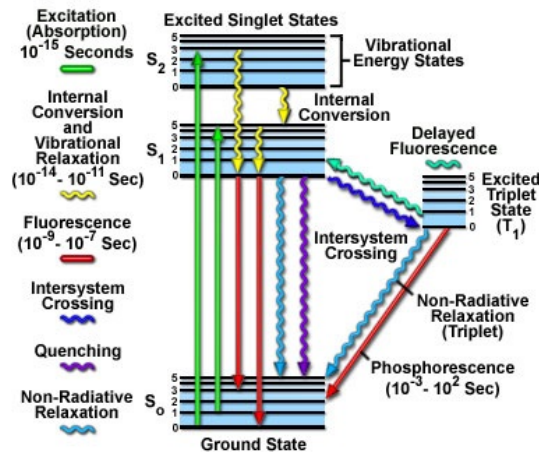
Figure 1.3: The Jablonski diagram. A picture of the Jablonski diagram, which schematically represents the many processes of energy conversion between molecular states after photon absorption: horizontal lines represent the electronic energy levels, while arrows represent excitation and relaxation processes. The energy levels are grouped into electronic states composed by multiple vibrational states [19].

In vibrational relaxation and internal conversion, the excited electron ceases part of its energy to other electrons of the same molecule, moving to lower energy vibrational and electronic states, respectively; in these cases the energy is released through heat.

In intersystem crossing to the triplet state, the excited electron, after a spin flip, cannot return to the ground state, and is therefore forced to decay to a more energetic level, i.e. the triplet state. From the triplet state, the electron can decay to the ground state either via phosphorescence (in certain conditions) or via other non-radiative processes. In any case, decay from the triplet state has characteristic times much longer than fluorescence.

Fluorophores are characterised by their excitation and emission spectra, both of which typically present a maximum. The wavelength corresponding to the maximum is called maximum excitation wavelength (Ex) for the excitation spectrum and maximum emission wavelength (Em) for the emission spectrum. Because of vibrational relaxation and internal conversion, Em is typically longer than Ex, and the difference between the two is called Stokes shift.
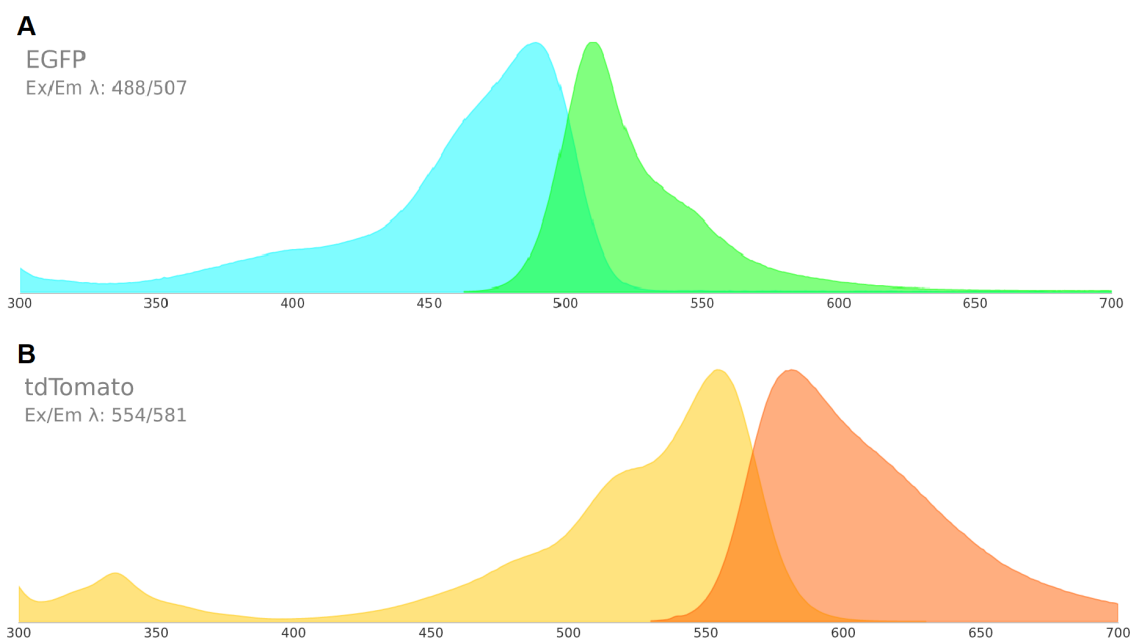
Figure 1.4: EGFP and tdTomato spectra. (A) Enhanced Green Fluorescent Protein's (26.9 kDa) excitation spectrum (blue) presents a peak at 488 nm, while the emission spectrum (green) presents a peak at 507 nm [20]. (B) Tandem dimer (td)Tomato's (54.2 kDa) excitation spectrum (yellow) presents a peak at 554 nm, while the emission spectrum (red) presents a peak at 581 nm [21].

The probability that a fluorophore will emit a photon after a photon has been absorbed is known as Quantum Yield (QY), a dimensionless number that is expressed as:

$$QY = \frac{\#\,emitted\ photons}{\#\,absorbed\ photons} \tag{1.2}$$

The Extinction Coefficient (EC) describes the reduction in light intensity per cm of penetration in a solution depending on the solution concentration (u.m.: $M^{-1}cm^{-1}$).

The product $b = QY \cdot EC$ defines the brightness of the fluorophore, while the actual intensity considers also the goodness of light collection:

$$I = I_0 \; k \; QY \; EC \; c \; l = I_0 \; k \; b \; c \; l \tag{1.3}$$

where I_0 is the source intensity, k is a parameter depending on the specific experimental apparatus describing how well it gathers light, c is the concentration and l is the light path length. Recalling that Beer-Lambert law states that $EC = \frac{A}{cl}$, with A being the absorbance of the solution, we can also rewrite equation (1.3) as $I = I_0 \; k \; QY \; A$.

1.3.2 Diffusion theory

Mass diffusion is the phenomenon by which a substance moves because of a concentration gradient.

Diffusion was quantitatively described by A. E. Fick (1855) through his laws, which link the diffusion flux $\mathbf{J}$ to the concentration gradient.

Fick's first law states:

$$\mathbf{J} = -D\nabla C \tag{1.4}$$

where $\mathbf{J}$ is the flux vector, C is the concentration and D is the diffusion coefficient. Assuming conservation of matter, one can then obtain Fick's second law:

$$\frac{\partial C}{\partial t} = D\nabla^2 C \tag{1.5}$$

2

Methods

2.1 Fluorescence Correlation Spectroscopy

Fluorescence Correlation Spectroscopy (FCS) is an experimental technique that allows to decipher the molecular dynamics of a sample – for example diffusion parameters – through the statistical analysis of the spontaneous fluctuations of its fluorescence signal at thermodynamic equilibrium. When a sample point is illuminated by, e.g., a laser, the molecules in the point-like detection volume emit a fluorescence signal; since the molecules in the sample move of Brownian motion, the number of molecules in the detection volume during the detection time will fluctuate, thus leading to fluctuations of the fluorescence signal, that are to be analysed.

FCS was first introduced in 1972 by Magde et al. [22] and since the beginning of the 1990s it has been largely exploited thanks to the implementation of confocal microscopy FCS by Rigler et al. [23], which pushed the sensitivity of the technique to the single-molecule level and allowed to extend its range of application. In particular, the information about the kinetics of the system is inferred by calculating and analysing the autocorrelation function of fluctuations in fluorescence emission.

Given the fluorescence signal $F(t)$, the autocorrelation function $G(\tau)$ relates the signal at time t to the signal at time $t + \tau$. Normalising by the mean fluorescence $\langle F(t) \rangle$ we obtain:

$$G(\tau) = \frac{\langle F(t)F(t+\tau) \rangle}{\langle F(t) \rangle^2} - 1 = \frac{\langle \delta F(t) \delta F(t+\tau) \rangle}{\langle F(t) \rangle^2} \tag{2.1}$$

with $\delta F(t) = F(t) - \langle F(t) \rangle$ being the deviation from the mean.

Since we are averaging over all time values, only those molecular processes that possess a characteristic relaxation time – e.g. chemical reactions or transport processes like Brownian motion – will eventually contribute to the autocorrelation function, while fluctuations with time constants that varies in time are averaged out and will not contribute.

Fitting the autocorrelation function by a formalism that describes the molecular processes that generate the fluctuations in the sample, we will obtain the parameters of dynamics looked for. In the case of Brownian motion, this formalism is represented by Fick's second law of diffusion, and we will obtain the diffusion coefficient.
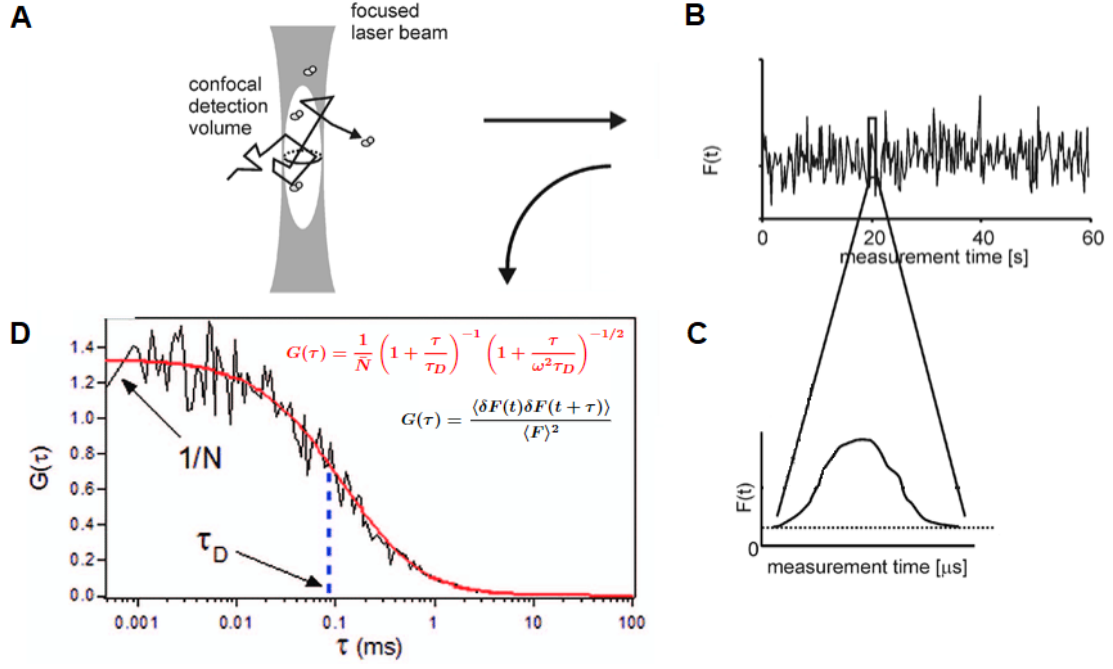
Figure 2.1: Overview of data analysis by means of FCS. When a fluorescent particle enters the detection volume (A), it causes a fluctuation in the fluorescence signal (B); in particular, the total fluorescence will increase of a quantity equal to the single molecule's fluorescence, for the time the particle remains within the detection volume (C). The resulting fluorescence signal over the whole measurement time will record every entering or exiting of fluorescent molecules in the detection volume. The signal is then processed by calculating its autocorrelation (D) and the resulting autocorrelation function is fitted by equation (2.8) [24, 25].

CALCULATIONS

Let's consider the case of one single species of fluorescent molecule in the sample, in conditions of normal diffusion [26]. The Brownian motion is then described by means of Fick's second law:

$$\frac{\partial \delta C(\vec{r}, t)}{\partial t} = D\nabla^2 \delta C(\vec{r}, t) \tag{2.2}$$

where $\delta C(\vec{r}, t) = C(\vec{r}, t) - \bar{C}$ is the local deviation of the concentration from its average value.

On the other hand, the fluorescence signal $F(t)$ depends both on fluorophore concentration in the detection volume and on the total intensity of the excitation light that hits the detection volume, at time t:

$$F(t) = g \; EC \; QY \int I(\vec{r}) \; C(\vec{r}, t) d^3 r \tag{2.3}$$

where g accounts for quantum efficiency, detector gain, and geometrical and filtering losses, QY is the fluorescence quantum yield and EC is the extinction coefficient.

Inserting the (2.3) into the (2.1) we will obtain:

$$G(\tau) = (g \; EC \; QY)^2 \int I(\vec{r})I(\vec{r'}) \; \langle \delta C(\vec{r}, t)\delta C(\vec{r}, t+\tau) \rangle \; d^3 r \; d^3 r' \tag{2.4}$$

8

The concentration is calculated solving the differential equation from (2.2) by taking a Fourier transform:

$$\delta C(\vec{q}, t) = \delta C(\vec{q}, 0) \exp(-Dq^2 t) \tag{2.5}$$

The excitation intensity, on the other hand, has to be calculated integrating the intensity distribution over the excitation volume, given by the Point Spread Function (PSF). Since the typical optical setup of the detection system is usually assumed to provide a three-dimensional Gaussian distribution, we will have:

$$I(\vec{r}) = I_0 \exp\left(-\frac{2(x^2 + y^2)}{w_{xy}^2} - \frac{2z^2}{w_z^2}\right) \tag{2.6}$$

with w_z and w_{xy} being the sizes of the beam waist in the direction of the propagation of light and in the perpendicular ones, respectively.

After inserting the (2.5) and the (2.6) into the (2.4) and integrating, we will obtain:

$$G(\tau) = \frac{1}{\bar{C}V}\left(1 + \frac{\tau}{\tau_D}\right)^{-1}\left(1 + \frac{\tau}{\tau_D'}\right)^{-1/2} \tag{2.7}$$

where $V = \pi^{3/2} w_{xy}^2 w_z$ is the detection volume, and $\tau_D = w_{xy}^2/4D$ and $\tau_D' = w_z^2/4D$ are the characteristic times of diffusion across and along the illuminated region, respectively.

We can rewrite (2.7) in an easier form, writing the average number of fluorescent molecules in the detection volume as $\bar{N} = \bar{C}V$ and defining $\omega = w_z/w_{xy}$:

$$G(\tau) = \frac{1}{\bar{N}}\left(1 + \frac{\tau}{\tau_D}\right)^{-1}\left(1 + \frac{\tau}{\omega^2 \tau_D}\right)^{-1/2} \tag{2.8}$$

Fitting the autocorrelation plot obtained by the data with function (2.8), we can eventually get the diffusion coefficient $D = w_{xy}^2/4\tau_D$. Notice that $\frac{1}{\bar{N}} = G(0)$, as we will refer to it in the future; this term is proportional to the fluorophore concentration, and the proportionality constant, in practice, has to be determined by means of a calibration.

From looking at the plot in figure 2.2, we can immediately observe that the higher the concentration, the flatter the curve, and therefore the less precise the characterisation of the system (i.e. the individuation, in experimental data, of the curve's inflection point). On the other hand, the slower the fluorophores, the more the curve will be right-shifted.
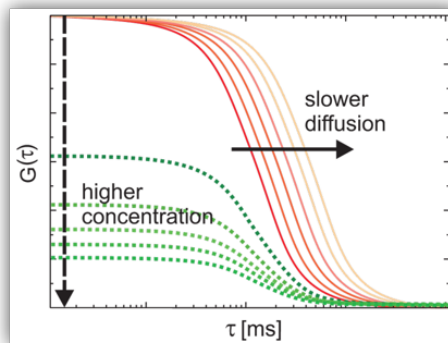
Figure 2.2: Autocorrelation function's shape in different conditions. $G(0)$ lowers at higher concentration, while τ_D increases at slower diffusion.

9

Some corrections can be applied to the 2.8, considering anomalous diffusion, chemical reactions, multiple fluorophores and triplet state correction, but they are not going to be considered in this preliminary work.

When employing FCS, in order to obtain a correct analysis we ought to make sure the following requirements are fulfilled:

- **low concentrations**. The fluctuation amplitude depends on the average number of fluorescent molecules in the detection volume. At too high concentrations, the fluorescence fluctuations will be indistinguishable from noise. Therefore, low numbers of molecule in the detection volume are mandatory, and these are achieved by concentrations in the low to medium nanomolar range [24];

- **thermodynamic equilibrium**. Being the technique based on the fluctuations around equilibrium, it is necessary that molecule concentrations and average mobilities remain constant for the time the recording is performed;

- **recording time and excitation power**. On the one hand, low concentrations extend the necessary measurement time: actually, with few molecular events per unit of time, longer times are required to get enough information on the system kinetic parameters. On the other, the requirement for stable equilibrium conditions together with photobleaching phenomenon limit the allowed recording time. Photobleaching is the inability of a fluorophore to fluoresce after it is photochemically altered; in other words, an excessive quantity of light hitting the fluorophore can chemically damage it and irreversibly modify its covalent bonds. To minimise photobleaching, the exciting light intensity and the excitation time must be appropriately set, so that the excitation power is high enough to properly excite the fluorophores while the total released energy is not high enough to cause significant photobleaching. In any case, the measurement time must be longer than the time constant of the slowest process investigated. For freely diffusing particles, a few seconds are usually sufficient to acquire an autocorrelation function [24].

2.2 RASTER IMAGE CORRELATION SPECTROSCOPY

Raster Image Correlation Spectroscopy (RICS) was developed by Digman et al. in 2005 [27]. In RICS, a stack of 2D rectangular images of a portion of the sample is collected via a raster scan (figure 2.3, panel B); every image is composed of a certain number of pixels, each one containing the light information collected from a point-size detection volume in a defined time interval, called pixel dwell time. When the collection of an image is completed, the system returns to the first position and another image is acquired.
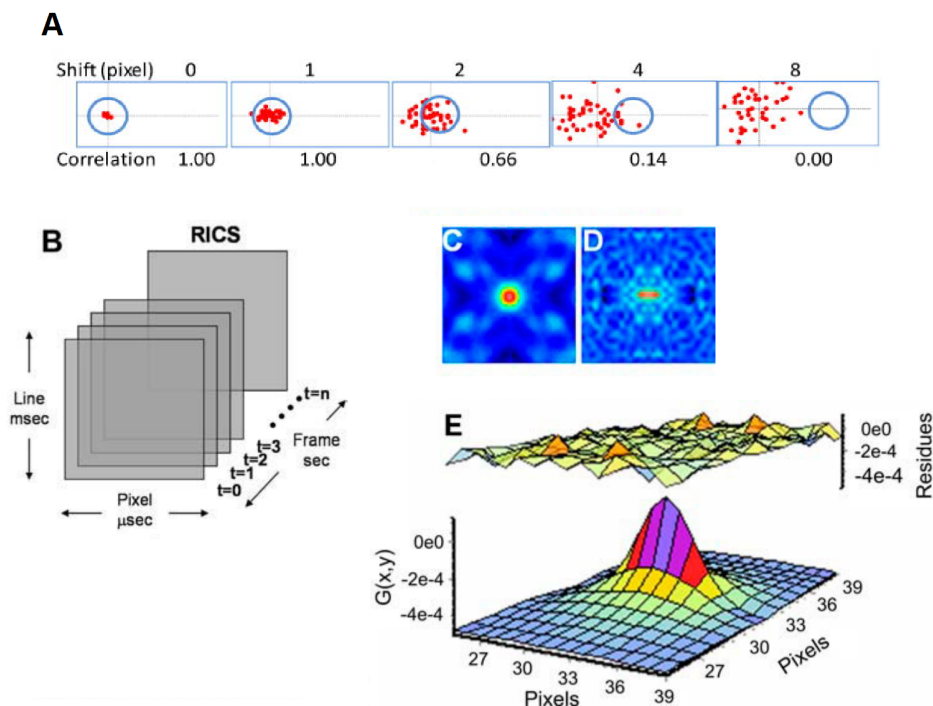
Figure 2.3: Overview of data analysis by means of RICS. (A) In the figure, the red dots represent molecules diffusing in a plane. As a function of time, molecules spread from the initial position. The fluorescence intensity is collected in sequence of neighbour pixels. As the molecules move and the pixel position is changed, only the molecules that can move fast enough will be observed at a distant pixel of the same image frame; therefore the correlation between pixels decreases with their relative distance. Since we are averaging over all spatial values, only the signal coming from the same molecule gives a net positive correlation between two different pixels [28]. (B) Visualisation of the 2D stack of images from raster scanning employed in RICS analysis. The pixel dwell time is typically of a few μs; as a consequence, the line time is in the order of ms and the total stack acquisition is in the order of s [27]. (C, D and E) Example of RICS analysis on a portion of a CHOK1 cell expressing paxillin-EGFP [27], with spatial autocorrelation before (C) and after (D) subtraction of immobile structures. In (E), fit of the spatial correlation function obtained in (D).

The information on diffusivity is obtained performing a spatial autocorrelation, by comparing the original image (seen as an intensity matrix of pixels) to all possible combinations of spatially shifted images [27]:

$$G(\xi, \psi) = \frac{\langle I(x,y)I(x+\xi, y+\psi)\rangle_{x,y}}{\langle I(x,y)\rangle_{x,y}^2} \tag{2.9}$$

Using this method, fluorescent molecules of the right characteristic time are "followed" by the laser to adjacent points (figure 2.3, panel A). This is possible because all pixels forming the image are acquired at a different times.

Each image provides one estimate of the spatial correlation (figure 2.3, panel C). The sequence of images is then used to improve the S/N ratio and to remove immobile fraction and slowly moving components (figure 2.3, panel D): from the temporal series of each pixel, a moving average is subtracted, then the average of the entire series is summed again to avoid division by zero in the autocorrelation calculations. Thanks to this procedure, the brighter zones are removed.

The obtained 2D matrix is eventually fitted by the following function (figure 2.3, panel E):

$$G_{RICS}(\xi, \psi) = S(\xi, \psi)G(\xi, \psi) \tag{2.10}$$

with $S(\xi, \psi)$ being the spatial correlation function related to scanning optics and $G(\xi, \psi)$ the spatial correlation function related to molecular dynamics. These are given by:

$$S(\xi, \psi) = \exp\left(-\frac{\frac{1}{2}\left(\frac{2\delta}{w_{xy}}\right)^2 (\xi^2 + \psi^2)}{1 + \frac{\tau_p \xi + \tau_l \psi}{\tau_D}}\right) \tag{2.11}$$

$$G(\xi, \psi) = \frac{1}{\bar{N}}\left(1 + \frac{\tau_p \xi + \tau_l \psi}{\tau_D}\right)^{-1}\left(1 + \frac{\tau_p \xi + \tau_l \psi}{\omega^2 \tau_D}\right)^{-1/2}$$

where $\bar{N}$ is the average number of particles in the excitation volume, δ is the pixel size, w_{xy} is the beam waist, τ_p is the pixel dwell time and τ_l the time between lines. Moreover, as in FCS, $\tau_D = w_{xy}^2/4D$ and $\omega = w_z/w_{xy}$.
Finally, from the fit we can obtain the diffusion coefficient.

ADVANTAGES WITH RESPECT TO FCS

As previously explained, the intracellular environment is complex and heterogeneous, rich in solutes and larger molecules. Macromolecules are often bound to each other through non-covalent interactions, such as hydrophobic effect, hydration and electrostatic interactions. The cytoplasm becomes thus structured into regions of crowded macromolecules and aqueous reservoirs with quasi-bulk concentrations of ions and compounds of (tipically) lower molecular weight (figure 1.2, panel C). It is then clear that, depending on the point within the cell chosen for the measurement, very different values for the diffusion coefficient can be obtained. Moreover, since intracellular anchors and crowded aggregates are constantly moving during the recording, the values of GFP concentration and diffusivity could noticeably vary, thus making it impossible to obtain a reliable value for the diffusion coefficient. In addition, there is the possibility that an organelle transits in the zone of interest during acquisition, which would bring to the same critical issues.

Therefore, when employing FCS many different points from the same cell must be sampled to obtain a reliable average value, strengthening the validity of the measurement, and it has to be checked that the fluorophore concentration does not noticeably vary.

On the other hand, RICS offers a more solid method for the determination of the diffusion coefficient with respect to FCS, since it samples many points at the same time. This allows to get much more information that FCS in the same time and to automatically study the average diffusion coefficient of a wide region. This makes the measure less subject to local variation in molecular crowding, quickly providing a picture of its average value in the whole cell. In any case, the acquisition region must be

placed as far as possible from the nucleus and the membrane, and the passage of big organelles must be checked.

2.3 THE CONFOCAL MICROSCOPE

The typical setup for fluorescence imaging consists of a light source, in our cases a laser, a microscope and one or more cameras or detectors. The laser emits a monochromatic light beam, whose intensity is regulated via an intensity modulation unit, typically an electro-optic or an acousto-optical modulator. The beam is then routed by means of mirrors along the optical path to the scan head of the microscope. Here, galvo mirrors allow the regulation of the beam direction on the specimen – permitting the scanning of a large portion of the sample point by point on the xy plane – and a telescope composed by a scan lens and a tube lens regulates the beam diameter in order to adapt its size to the objective's pupil dimension.
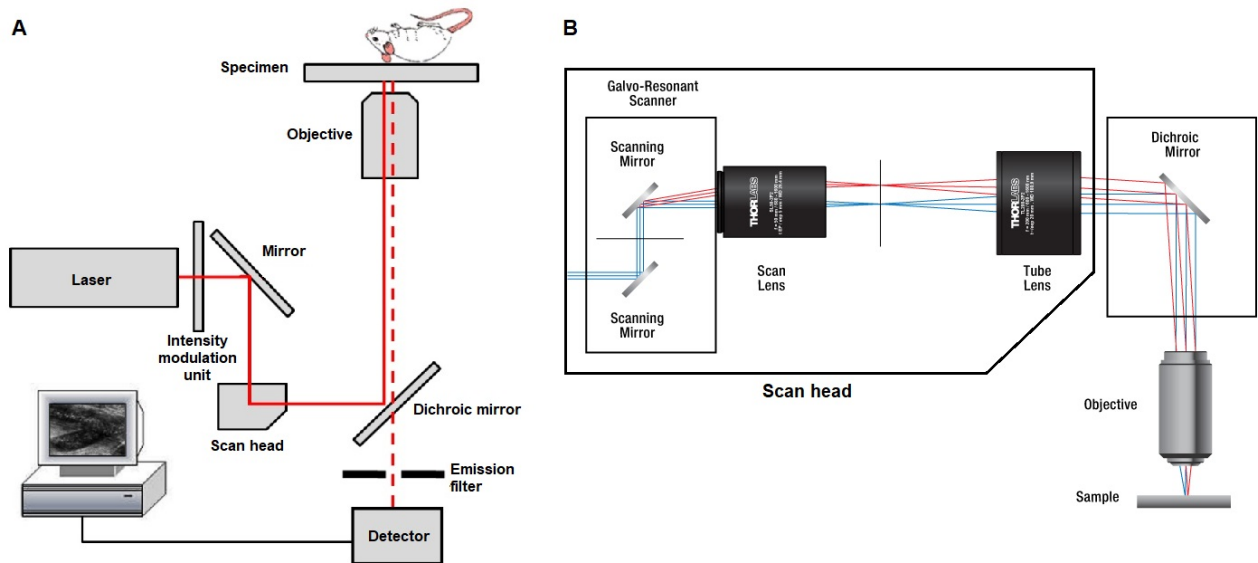
Figure 2.4: Confocal microscope setup. (A) Schematic of the setup of an inverted confocal microscope. Adapted from [29]. (B) Zoom on the scan head, with schematic representation of the principle of galvo mirrors [30]

From the objective, the beam is projected onto the sample plane, where it excites the fluorescent molecules. The light emitted by these molecules is then collected by the same microscope objective, travelling in the opposite direction with respect to the exciting light. Before the objective, an appropriately designed dichroic mirror separates the exciting light from the emitted one: it works as a transmitting window for wavelengths in a defined band and as a mirror for wavelengths in a different band. It is typically characterised by a cutoff wavelength, reflecting all the wavelengths longer than it while allowing the passage of the shorter ones – or vice versa. In this way, the emitted light beam, after being possibly split again by means of one or more additional dichroic mirrors, can be directed towards the detectors – usually PhotoMultiplier Tubes (PMTs) or PhotoDiodes (PD) – that convert light into an electric current. In front of the detector, an emission wavelength filter is positioned to reject light outside the desired emission band.
The current signal recorded by the detectors is then processed by the acquisition electronics that, after amplification and digitisation, sends the resulting electronic signal to the computer for the analysis.

In a confocal microscope, even if the laser light is concentrated on a specific point of the sample, the

actual illumination region has the shape of a double cone: all parts of the sample within the illumination region are uniformly excited at the same time, throughout the whole specimen's thickness. As a consequence, a large part of the unfocused background fluorescence is detected, and secondary fluorescence originating from areas above and below the focal plane will further disturb the measurement, resulting in a significant loss of resolution and contrast.

To overcome this problem, a couple of pinholes is introduced: one positioned after the intensity modulation unit and one in front of the detector. In particular, the latter strongly limits the collection of light from unwanted regions. Indeed, points above and below the focal plane are not confocal with the pinhole, therefore only a small fraction of the unfocused fluorescence emission is delivered through the pinhole aperture, and the detected light will almost uniquely come from the point-like focused volume. On the other hand, since most of the light is blocked at the pinhole, the signal intensity is decreased, thus requiring longer integration.
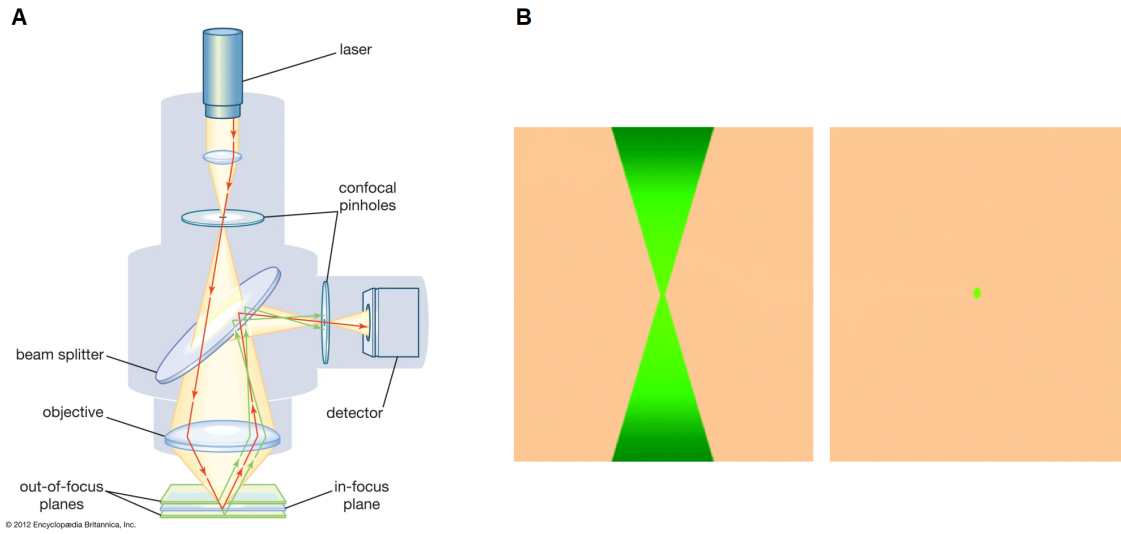
Figure 2.5: Confocal principle. (A) Schematic of the confocal microscope principle, with operation principle of pinholes [31]. (B) Representation of the illuminated region around the focused sample plane in a confocal microscope (left) and actual region detected thanks to pinholes (right).

When talking about a point-like illumination volume, we obviously have to take into account the resolution limits of the system, which determine the minimum dimension of this volume. The minimum resolvable distances on the xy plane and in the z direction are known as Abbe's diffraction limits and can be estimated from the Rayleigh criterion, which states:

$$
\begin{aligned}
d_{xy} &= \frac{\lambda}{2NA} = \frac{\lambda}{2n sin\theta} \\
d_z &= \frac{2\lambda}{NA^2} = \frac{2\lambda}{(n sin\theta)^2}
\end{aligned}
\tag{2.12}
$$

where λ is the wavelength of the incident light, NA is the numerical aperture of the objective, n is the refraction index of the medium in which the objective is working and θ is the maximum half-angle of the cone of light that can enter the lens.

Assuming a typical 500 nm light wavelength and a numerical aperture of 1.2, we can obtain a rough yet indicative value of $d_{xy} \approx 200$ nm and $d_z \approx 700$ nm (in general we will typically have $d_z \approx 3.5 \cdot d_{xy}$ for a confocal microscope).

2.4 Towards *in vivo* measurements of molecular crowding: the two-photon microscope

In vivo measurements are to be performed on mice genetically modified to express free GFP in neurons. To uncover the brain, a portion of the mouse's skull is removed and, if necessary, replaced by a coverslip fixed by means of cement.

When performing *in vivo* measurements, it is necessary to excite at greater depths, since the most superficial pyramidal neurons are located at approximately 100 μm from the brain surface [32], under the first superficial layer of the cortex. Confocal microscopy, which employs visible light, is limited to roughly less than 100 μm in penetration; therefore, it is not suitable for *in vivo* measurements.

The solution comes from two-photon microscopy, first developed by Denk et al. in 1990 [33], that exploits the "optical window" of cells and tissues (i.e. the 650 - 900 nm wavelength range [34], see figure 2.6 panel C), allowing penetration depths of a few millimeters [35] to a few centimeters [34] in most tissues.
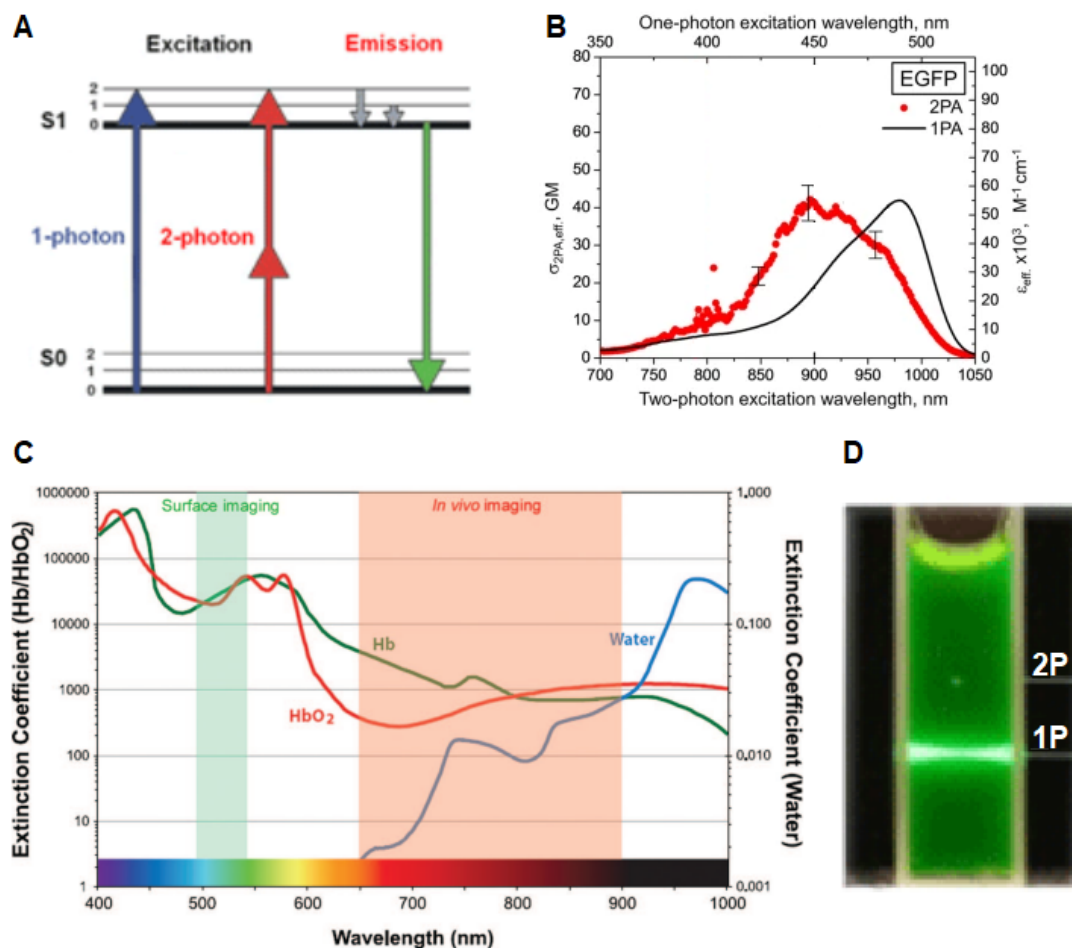
Figure 2.6: Overview of two-photon microscopy. (A) Two-photon excitation principle, compared to single-photon. The green line represents energy release by fluorescence, grey lines represent energy release by non-radiative processes [36]. (B) Two-photon absorption cross section (red symbols) with 10% error (black error bars) and one-photon extinction (black solid lines) of EGFP [37]. (C) The "optical window" of cells, where photon absorption by the major intracellular absorbers (water and blood, namely oxy- and deoxyhemoglobin) is low [38]. (D) Comparison of the excitation volume in two-photon (point-like volume) and one-photon microscopy (double cone of excitation).

While the excitation spectrum of most fluorophores lays in the visible range – and therefore one-photon stimulation in the optical window would not produce a significant fluorescence – with two-photon excitation it is possible to obtain an efficient stimulation using photons of longer wavelength. Indeed, two photons can be absorbed by a fluorescent molecule at the same time, so that the total absorbed energy is given by the sum of the energies of the two photons (figure 2.6, panel A). Since the energy of a photon follows the Planck-Einstein relation $E = h\nu = hc/\lambda$, the two photons will have a wavelength longer than the one of photons in one-photon excitation. In particular, in two-photon microscopy the two exciting photons come from the same laser, hence have the same wavelength; their effect will be the same of that of a single photon of half the wavelength of the two photons.

A further advantage of 2-p microscopy, apart from deeper penetration, is that it is intrinsically confocal: the excitation volume is a naturally 3D-Gaussian-shaped volume, with no double cone that penetrates the entire specimen, so no pinhole is necessary (figure 2.6, panel D). In particular, recalling equation (2.12), for a typical 900 nm excitation light and a 1.0 numerical aperture (water immersion) we will have $d_{xy} \approx 350$ nm and $d_z \approx 1250$ nm.

Finally, being the excitation light less energetic, the sample is less subject to photodamage and photobleaching.

2.5 Experimental setup

The microscope was kindly placed at our disposal by Prof. Cardarelli. It is an Olympus Fluo View 1000 inverted confocal microscope, i.e. the excitation beam comes from below the specimen and the emitted light is collected from below as well. The laser and microscope setup, as well as the data acquisition, were performed thanks to the FV-1000 software.

Figure 2.7: Olympus Fluo View 1000 [39].

2.5.1 Considerations

Photon counting mode. While a normal photodetector generates an analogue signal proportional to the number of incident photons, in photon counting mode the photodetector generates a pulse signal every time a single photon is detected; thus, counting the number of pulses in the unit of time we will have the number of photons arriving on the detector. Amongst the main advantages of employing photon counting mode is the elimination of the gain noise, thus increasing the total signal-to-noise ratio. Moreover, temporal resolution is improved, since the time arrival of photons can be determined more precisely from pulse signal. These advantages are essential when performing FCS, where we are working with low intensity signal and a it is necessary to precisely identify the time of photons arrival to perform a good autocorrelation. On the Olympus, photon counting mode is available and is performed directly by PMTs.

Estimation of the PSF dimensions. As we have seen in equation (2.8), the PSF dimensions appear in the autocorrelation function. Even if they could be obtained through the fitting, since the data is quite noisy and imprecise and since the PSF dimensions are constant over time, we would better fix their values, so that we will have only two parameters to infer from the fit ($G(0)$ and τ_D). Actually, the PSF dimensions are usually calculated by means of a calibration performed by means of an FCS measurement of a homogeneous solution of fluorophores of precisely known diffusivity. In practice, in our case the calibration was not executed and the values were calculated through the estimation that was previously performed using equations (2.12): $d_{xy} \approx 20$ nm and $d_z \approx 700$ nm, with $\omega \approx 3.5$.

2.6 Procedure

2.6.1 Cell preparation

Since we were using an inverted microscope, cells were prepared in a dish with a thin polymeric bottom, easier to be crossed by the excitation light and usable also with an immersion objective and at short working distance.

Cells were kindly prepared by other researchers from the laboratory, according to the procedure that is now presented.

Cell culture

Neuro2A cells were cultured in DMEM complete medium supplemented with FBS 10%, L-Glutamine 1%, HEPES 1%, Pen/Strep 1%. Cells were splitted every 2-3 days when they reached 90% confluence. During the splitting procedure, cells were washed once with PBS solution without Ca^{2+} and Mg^{2+}, then incubated with 1 ml Trypsin-EDTA at 37°C for 3 mins. After the incubation, an equal amount of DMEM complete medium was added to the cells, to block the trypsin reaction. The cells were then detached, by gently pipetting with p1000 pipette. The solution of detached cells was transferred to a 15 ml falcon tube and PBS solution without Ca^{2+} and Mg^{2+} was added to a final amount of 10 ml. Cells were then centrifuged at 200 g for 5 mins. The supernatant was discarded and DMEM complete medium was added, in order to resuspend the cells. Cells were then replated according to their amount, so that the following day they were around 50% confluent. For the imaging experiments, cells were plated on WillCo. wells cell plates HBST-3512, whereas for cell maintenance p60 cell plates (tissue culture treated by vacuum gas plasma) were used.

Cell transfection
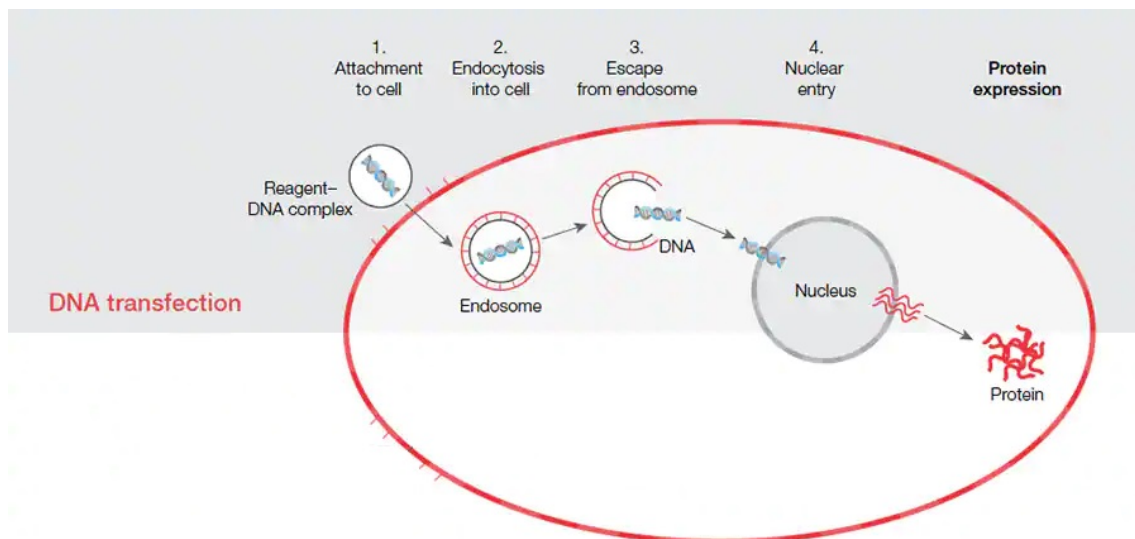
Figure 2.8: Cell transfection. Schematic of the main phases of cell transfection by means of liposomes. Adapted from [40].

Cells were transfected with either EGFP or tdTomato at around 90% confluence, with Lipofectamine 2000 (Invitrogen) as described in the manufacturer's protocol. In brief, for each construct 2 μg of

19

DNA were resuspended in 100 μL of Optimem (Invitrogen) and, in a separate 1.5 μL tube, 4 μL of Lipofectamine 2000 were resuspended in 100 μL of Optimem. Solutions were then let to settle for 5 mins, and subsequently mixed together. Then the obtained transfection solution was let to settle for 15 mins. Finally, cells were washed twice with PBS without Ca^{2+} and Mg^{2+} and the transfection solution was applied. We waited 15 mins for the solution to transfect the cells and then we added the DMEM complete medium and placed cells back in the incubator.

2.6.2 MEASUREMENTS

A Leica, 63× oil-immersion objective was employed. A drop of oil was positioned on the objective by means of a pipette, then the dish was put in place into the microscope and the objective was moved towards the dish until the oil got in touch with the dish. Oil is used in place of water because with its higher refractive index it increases the numerical aperture of the objective (see equation 2.12).

The specimen was focused looking into the oculars using transmitted light. Then laser scanning was activated and the cells to be utilised for the measurements were chosen following the requirements previously described, i.e. the least expressing ones were preferred.

For EGFP measurements, the laser wavelength was set to 488 nm, and its power regulated approximately in the 0-100% range so that the fluorescence level looked optimal. An excitation filter, a dichroic filter and an emission filter were selected. The latter is an opto-acoustic filter set to 500 nm with 100 nm range (it accepts light from 450 to 550 nm). The same was done for tdTomato measurements, setting the excitation wavelength to 543 nm and the filter to 560 nm with 60 nm range. Then the PMTs were selected, set up in photon-counting mode and with gain to 700 V.

The acquisition points (for FCS) and regions (for RICS) were placed within the cytoplasm, far enough from both the nucleus and the membrane, so that movements of these structures did not affect the measurements.

For FCS measurements, we collected data from 10 different points belonging to 2 different cells expressing EGFP. The sampling speed was set to 2 μs per pixel, for a total acquisition of about 17 s (8388608 pixels).

RICS measurements were performed on both cells expressing EGFP and tdTomato: the data for EGFP were collected from 11 different regions belonging to 4 different cells, and for tdTomato from 20 different regions belonging to 12 different cells. The acquisition regions had dimensions of 13×13 μm (256×256 pixels). The sampling speed was set to 2 μs per pixel, and for every region a stack of 200 frames was collected, for a total acquisition of about 85 s.

<div style="text-align: right; font-size: 3em;">3</div>

Results

The data was analysed with the program *SimFCS 4.0* developed by Enrico Gratton. A release of the program is available at the link `https://www.lfd.uci.edu/globals/`.

3.1 FCS

During acquisition, the data is stored in a TIF file as a rectangular image of pixels, each one containing the information collected in the 2 μs pixel dwell time from a PSF-size volume.

The data was then divided into slots of about 250 ms, that were averaged out to remove as much noise as possible.
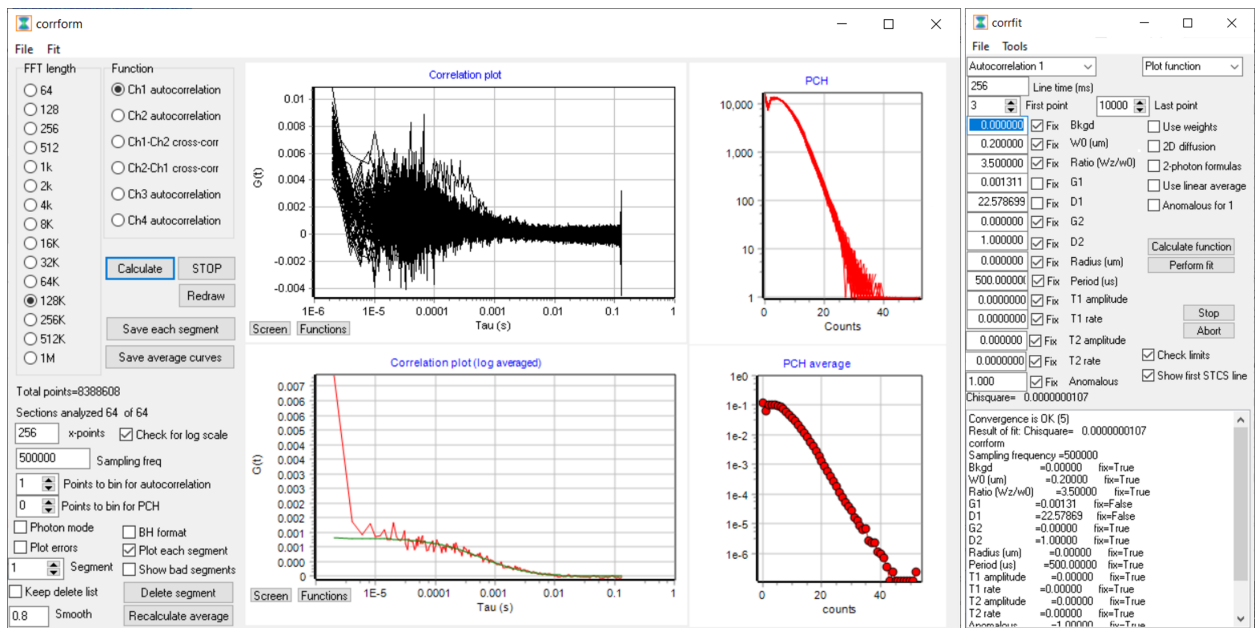
Figure 3.1: SimFCS 4.0. A window of the program to analyse the FCS data. Here, analysis of point 4 from cell 2 is shown. (Left window) On the left panel, plot options can be selected: sampling frequency, length of each segment, plot each segment. At the centre, the correlation curves of each segment (above) and their average (below) are plotted. The green line represents the fit. (Right window) Fit options and commands.

The program allows to perform the fit on the average curve and returns the diffusion coefficient $D1$, the intercept $G1$ and the background. The background was usually set to 0, to leave only two parameters to be calculated by the fit. W_0 (aka w_{xy}) was set to 200 nm and the $Ratio(Wz/w0)$ (aka $\omega = w_z/w_{xy}$) to 3.5. As it can be seen in the image, the very first points assume very high values (shot noise), because

<div style="text-align: center;">21</div>

if the time series is shifted of few microseconds with respect to itself, the autocorrelation will result to be very high – and very far from theoretical expectations. The influence of these points on the fit is then removed by applying an option ("First point" in figure 3.1, right window) that allows to exclude them.

We obtained the following results:

Cell	Point	D (μm^2/s)	Mean (μm^2/s)	STD (μm^2/s)
1	1	54.9	35	26
	2	39.0		
	3	63.8		
	4	6.2		
	5	11.4		
2	1	38.5	24	14
	2	18.5		
	3	4.3		
	4	22.6		
	5	34.0		

Table 3.1: Data from FCS on Neuro2A cells. Mean and standard deviation for the two cells are also displayed.
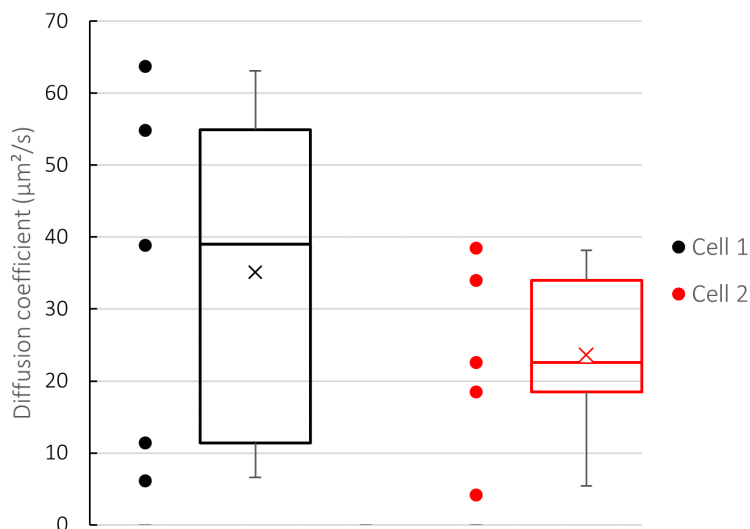
Figure 3.2: Results for the FCS measurements of EGFP diffusion coefficients.
The box indicates the median (central line) and the 1st and 3rd quartiles (bottom and top line). The dots indicate all the values, the cross within the box indicates the mean value, and the whiskers indicate the 2nd and 98th quartiles.

All values fall approximately in the 4 - 64 μm^2/s range. The average diffusion coefficient values for the two cells result to be 35 ± 11 μm^2/s and 24 ± 6 μm^2/s, with a total, average value of 29 ± 6 μm^2/s (standard deviation of 20 μm^2/s).

First of all, it can be immediately observed the data range – as well as the standard deviation – be quite wide. This can be easily explained thanks to the considerations already pointed out: the cell is a complex environment and diffusion coefficient values are very different at different points within the cell. However, all values make sense for an eukaryotic cell. In particular, the mean values 35 and 24 μm^2/s

are comparable to the ones found in literature. Actually, regardless of the method employed to make the measurements, diffusion coefficient values of GFP and EGFP in cells are widely assessed to be in the 20 - 30 μm^2/s range. By way of example, we report 20 to 25 μm^2/s in Neuro2A cells [18], 22.6 ± 3.7 μm^2/s in HeLa cells [16], 21.9 ± 7.2 μm^2/s in CHO-K1 cells [14], and measurements for many other cells are available [12, 13, 15, 17].

Concentration values (from $G(0)$) were not taken into account since a calibration would have been necessary to critically evaluate them; as previously explained, this was not carried out since it lies outside the objectives of this preliminary measurements.

3.2 RICS

The data was stored into a series of TIF files, each one containing the data for one image of the stack. The stack was used to remove the immobile fraction by setting a moving average every 2 frames. Then the fit was performed setting the same parameters used in FCS.

We obtained the following results:

Cell	Trial 1	Trial 2	Trial 3	Mean
1	34.8	26.0	20.6	27.1
2	7.8	18.4		13.1
3	29.9	21.2	31.6	27.6
4	20.3	27.5	18.3	22.0

| Cell	Trial 1	Trial 2	Trial 3	Mean
1	7.5			7.5
2	10.8			10.8
3	**3.2**			-
4	21.9	19.0		20.4
5	8.3	6.4		7.3
6	1.4	**$3 \cdot 10^9$**		1.4
7	8.1	16.1	9.3	11.1
8	22.0	12.7		17.3
9	14.1	14.1		14.1
10	4.4	12.9		8.6
11	7.9			7.9
12	4.4	12.4		8.4

Table 3.2: Data from RICS for EGFP (above) and tdTomato (below) in Neuro2A cells. All values are meant in μm^2/s. Highlighted values were discarded.

For tdTomato, cell number 3 and trial 2 from cell number 6 were excluded. Actually, in cell nr. 3 some macro structures – probably organelles – could be observed to move within the observed region while for cell nr. 6 the value of $3 \cdot 10^9$ is a clear outlier, probably due to an error in data acquisition or storage.

EGFP data is all in the 7.8 - 31.6 μm^2/s range, and the total mean gives a value of 23 ± 2 μm^2/s, with an 8 μm^2/s standard deviation. First of all, this value is comparable with the ones obtained through FCS and finds confirmation in literature.

On the other hand, once excluded cell 3 and trial 2 from cell 6, tdTomato data is all in the 1.4 - 22 μm^2/s range, and the total mean gives a value of 11 ± 1 μm^2/s, with a 6 μm^2/s standard deviation. Even

though we are not aware of previous estimates in literature of the diffusion coefficient of free tdTomato in cell – being it usually employed bound to other structures – we could expect a smaller value than EGFP, since it is about twice as heavy, in line with what we have obtained.
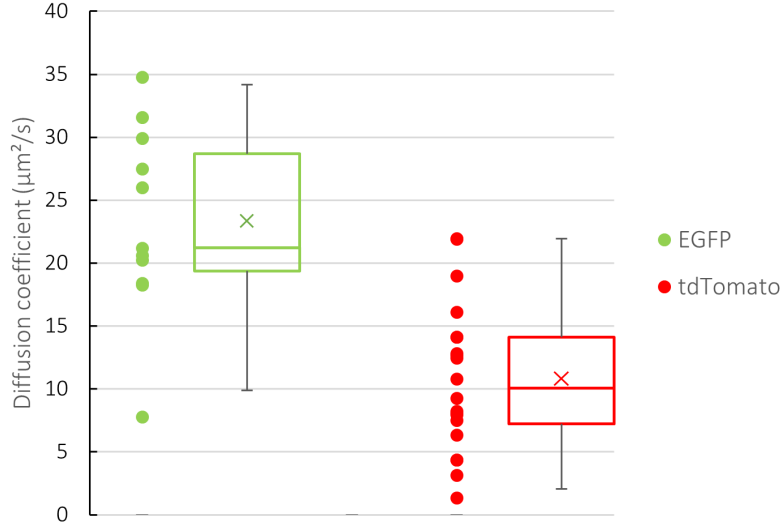
Figure 3.3: Results for the RICS measurements of EGFP and td-Tomato diffusion coefficients. The plot is designed as in figure 3.2.

Indeed, we can estimate the diffusion coefficient of a spherical particle from the Stokes-Einstein relation:

$$D = \frac{k_B T}{6\pi\eta R} \tag{3.1}$$

where k_B is the Boltzmann's constant, T is temperature, η is the dynamic viscosity of the medium and r is the particle's radius. Assuming the molecules of the two fluorophores to be spherical and considering temperature and viscosity to be the same in all measurements, we would obtain:

$$\frac{D_{Tomato}}{D_{EGFP}} = \frac{R_{EGFP}}{R_{Tomato}} \tag{3.2}$$

Assuming the molecular densities of the two fluorophores to be the same and to be uniform in the spheres, we should have:

$$\frac{R_{EGFP}}{R_{Tomato}} = \left(\frac{M_{EGFP}}{M_{Tomato}}\right)^{1/3} \approx \left(\frac{1}{2}\right)^{1/3} \approx 0.8 \tag{3.3}$$

with M being the mass, and therefore $D_{Tomato} \approx 0.8 \cdot D_{EGFP} \approx 18 \ \mu\text{m}^2/\text{s}$. However, since the assumptions made on the sphericity of the molecules are far from reality (see figure 3.4), the obtained value of 11 $\mu\text{m}^2/\text{s}$ could easily be plausible as well.
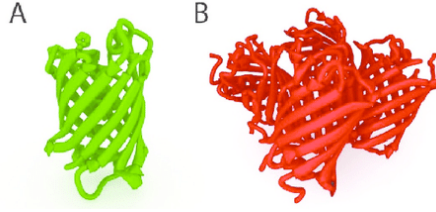
Figure 3.4: EGFP and tdTomato molecules. Simulation of the shape of EGFP (A) and tdTomato (B) molecules [41].

3.3 COMPARISON

The standard deviation of EGFP diffusivity obtained by means of RICS analysis is about 2.5 times smaller than the one obtained with FCS, confirming the averaging action of the RICS technique on a large portion of the cell (figure 3.5). Moreover, the amount of information collected in the same time was much larger ($256 \times 256 \approx 65,000$ points vs 1 point), allowing to quicken the measurement procedure and to obtain more reliable values of the average diffusivity within the cell.

We then demonstrated that RICS could be preferable to FCS for this kind of measurements.
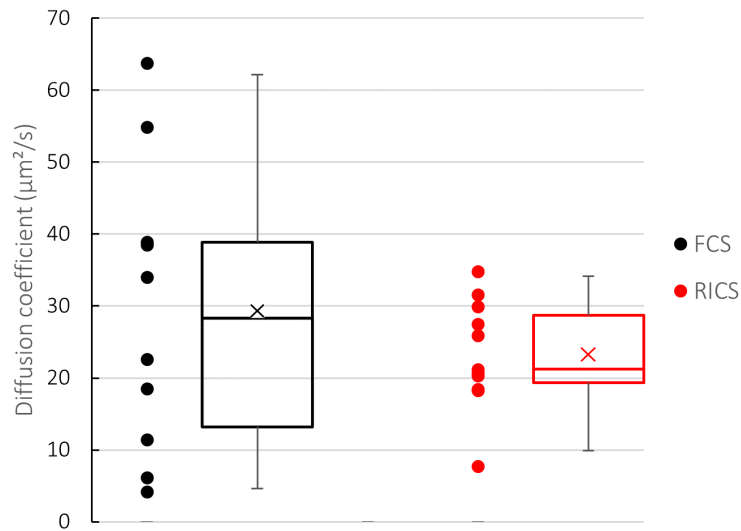
Figure 3.5: Comparison between FCS and RICS results. The plot is designed as in figure 3.2.

4
Conclusions

In this project, we aimed at tackling the problem of measuring molecular crowding in living cells *in vitro* by means of non-invasive techniques. We therefore applied fluctuation spectroscopy techniques, namely FCS and RICS, to measure the average intracellular diffusion coefficient of free EGFP and tdTomato, collecting data from transfected Neuro2A cells by means of a standard confocal microscope. For EGFP, we obtained results in accordance with known values from literature through both techniques. We were also able to establish the advantages offered by RICS with respect of FCS for this kind of measurements; in particular, the standard deviation of RICS measurements was significantly lower than the standard deviation of FCS measurements, confirming its averaging action, essential when probing a heterogeneous environment like the eukaryotic cytoplasm. Results for tdTomato, even if no reference value is available in literature, were considered plausible in the light of its structure. In the future, some improvements could be implemented to obtain more reliable values: calibration and evaluation of concentration, calibration of the PSF, check that the temperature remains constant for all acquisitions, use of corrected formulas to take into account anomalous diffusion and triplet state.

In further work, the tested procedures may be applied to assess the existence and the characteristics of the circadian rhythm of molecular crowding in neuronal cells, both *in vitro* and *in vivo*, and to compare it to the already assessed circadian rhythm of Cl^-, searching for correlations and, hopefully, getting a better understanding of its control mechanisms.

Acknowledgments

References

[1]   Maset A, Galla L, Francia S, Cozzolino O, Capasso P, Goisis RC, Losi G, Lombardo A, Ratto GM, Lodovichi C. Altered Cl- homeostasis hinders forebrain GABAergic interneuron migration in a mouse model of intellectual disability. Proc Natl Acad Sci U S A. 2021 Jan 12;118(2):e2016034118. doi: 10.1073/pnas.2016034118.

[2]   Pracucci, E.; Grahm, R.; Alberio, L.; Nardi, G.; Cozzolino, O.; Pillai, V.; Saieva, S.; Walsh, D.; Pasquini, G.; Landi, S.; Zhang, J.; Trevelyan, A.J.; Ratto, G.M. (2021). Circadian rhythm in cortical chloride homeostasis underpins variation in network excitability. BioRχiv. doi.org/10.1101/2021.05.12.443725.

[3]   Stangherlin, A.; Watson, J.L.; Wong, D.C.S. et al. (2021) Compensatory ion transport buffers daily protein rhythms to regulate osmotic balance and cellular physiology. Nat Commun 12, 6035. doi:10.1038/s41467-021-25942-4.

[4]   Swaminathan, R.; Hoang, C.P.; Verkman, A.S. (1997). Photobleaching recovery and anisotropy decay of green fluorescent protein GFP-S65T in solution and cells: cytoplasmic viscosity probed by green fluorescent protein translational and rotational diffusion. Biophysical Journal, 72(4), 1900–1907. doi:10.1016/s0006-3495(97)78835-0.

[5]   Mourão, Márcio A.; Hakim, Joe B.; Schnell, Santiago (2014). Connecting the Dots: The Effects of Macromolecular Crowding on Cell Physiology. Biophysical Journal, 107(12), 2761–2766. doi:10.1016/j.bpj.2014.10.051.

[6]   Rivas, Germán; Minton, Allen P. (2016). Macromolecular Crowding In Vitro, In Vivo, and In Between. Trends in Biochemical Sciences, (), S096800041630130X–. doi:10.1016/j.tibs.2016.08.013.

[7]   McGuffee, Sean R.; Elcock, Adrian H.; Briggs, James M. (2010). Diffusion, Crowding Protein Stability in a Dynamic Molecular Model of the Bacterial Cytoplasm. PLoS Computational Biology, 6(3), e1000694–. doi:10.1371/journal.pcbi.1000694.

[8]   https://tengk.wordpress.com/2015/11/05/set-27-general-science-biology/.

[9]   Minton, A. P. (2001). The Influence of Macromolecular Crowding and Macromolecular Confinement on Biochemical Reactions in Physiological Media. Journal of Biological Chemistry, 276(14), 10577–10580. doi:10.1074/jbc.R100005200.

[10]   Spitzer, J. (2011). From Water and Ions to Crowded Biomacromolecules: In Vivo Structuring of a Prokaryotic Cell. Microbiology and Molecular Biology Reviews, 75(3), 491–506. doi:10.1128/MMBR.00010-11.

[11]   Alan S Verkman (2002). Solute and macromolecule diffusion in cellular aqueous compartments., 27(1), 27–33. doi:10.1016/s0968-0004(01)02003-5.

[12]   Gura Sadovsky, Rotem; Brielle, Shlomi; Kaganovich, Daniel; England, Jeremy L. (2017). Measurement of Rapid Protein Diffusion in the Cytoplasm by Photo-Converted Intensity Profile Expansion. Cell Reports, 18(11), 2795–2806. doi:10.1016/j.celrep.2017.02.063.

[13]   Swaminathan, R.; Hoang, C.P.; Verkman, A.S. (1997). Photobleaching recovery and anisotropy decay of green fluorescent protein GFP-S65T in solution and cells: cytoplasmic viscosity probed by green fluorescent protein translational and rotational diffusion. Biophysical Journal, 72(4), 1900–1907. doi:10.1016/s0006-3495(97)78835-0.

[14]   Hedde, Per Niklas; Stakic, Milka; Gratton, Enrico (2014). Rapid Measurement of Molecular Transport and Interaction inside Living Cells Using Single Plane Illumination. Scientific Reports, 4(), 7048–. doi:10.1038/srep07048.

[15]   Potma, Eric O.; Boeij, Wim P. de; Bosgraaf, Leonard; Roelofs, Jeroen; van Haastert, Peter J.M.; Wiersma, Douwe A (2001). Reduced Protein Diffusion Rate by Cytoskeleton in Vegetative and Polarized Dictyostelium Cells. Biophysical Journal, 81(4), 2010–2019. doi:10.1016/s0006-3495(01)75851-1.

[16]   Ruan, Qiaoqiao; Chen, Yan; Gratton, Enrico; Glaser, Michael; Mantulin, William W. (2002). Cellular Characterization of Adenylate Kinase and Its Isoform:Two-Photon Excitation Fluorescence Imaging and Fluorescence Correlation Spectroscopy. Biophysical Journal, 83(6), 3177–3187. doi:10.1016/s0006-3495(02)75320-4.

[17]   Partikian, A. (1998). Rapid Diffusion of Green Fluorescent Protein in the Mitochondrial Matrix. The Journal of Cell Biology, 140(4), 821–829. doi:10.1083/jcb.140.4.821.

[18]   Kitamura, Akira; Kinjo, Masataka (2018). Determination of diffusion coefficients in live cells using fluorescence recovery after photobleaching with wide-field fluorescence microscopy. Biophysics and Physicobiology, 15(0), 1–7. doi:10.2142/biophysico.15.0_1.

[19]   https://www.olympus-lifescience.com/es/microscope-resource/primer/java/jablonski/jabintro/.

[20]   https://www.fpbase.org/protein/R9NL8/.

[21]   https://www.fpbase.org/protein/PGG5S/.

[22]   Magde, Douglas; Elson, Elliot; Webb, W. W. (1972). Thermodynamic Fluctuations in a Reacting System—Measurement by Fluorescence Correlation Spectroscopy. Physical Review Letters, 29(11), 705–708. doi:10.1103/PhysRevLett.29.705.

[23]   R. Rigler; Ü. Mets; J. Widengren; P. Kask (1993). Fluorescence correlation spectroscopy with high count rate and low background: analysis of translational diffusion., 22(3), 169–175. doi:10.1007/bf00185777.

[24]   Hof, M.; Hutterer, R.; Fidler, V. (2005). [Springer Series on Fluorescence] Fluorescence Spectroscopy in Biology Volume 3 || Fluorescence Correlation Spectroscopy in Cell Biology., 10.1007/b138383(Chapter 14), 245–262. doi:10.1007/3-540-27004-3_14.

[25]   Godet, Julien; Mély, Yves (2010). Biophysical studies of the nucleic acid chaperone properties of the HIV-1 nucleocapsid protein. RNA Biology, 7(6), 687–699. doi:10.4161/rna.7.6.13616.

[26]   Krichevsky, Oleg; Bonnet, Grégoire (2002). Fluorescence correlation spectroscopy: the technique and its applications. Reports on Progress in Physics, 65(2), 251–297. doi:10.1088/0034-4885/65/2/203.

[27]   Digman, Michelle A.; Brown, Claire M.; Sengupta, Parijat; Wiseman, Paul W.; Horwitz, Alan R.; Gratton, Enrico (2005). Measuring Fast Dynamics in Solutions and Cells with a Laser Scanning Microscope. Biophysical Journal, 89(2), 1317–1327. doi:10.1529/biophysj.105.062836.

[28]   Michelle A. Digman; Enrico Gratton (2012). Scanning image correlation spectroscopy. , 34(5), 377–385. doi:10.1002/bies.201100118.

[29]   Choi, Sung Min; Kim, Wi Han; Côté, Daniel; Park, Cheol-Woo; Lee, Ho (2011). Blood cell assisted in vivo Particle Image Velocimetry using the confocal laser scanning microscope. oe/19/5/oe-19-5-4357.pdf, 19(5), 4357–0. doi:10.1364/OE.19.004357.

[30]   https://www.thorlabs.com/newgrouppage9.cfm?objectgroup_ID=11010.

[31]   Encyclopedia Britannica, inc.

[32]   Muñoz-Castañeda, R., Zingg, B., Matho, K.S. et al. Cellular anatomy of the mouse primary motor cortex. Nature 598, 159–166 (2021). https://doi.org/10.1038/s41586-021-03970-w.

[33]   Denk, W; Strickler, J.; Webb, W. (1990). Two-photon laser scanning fluorescence microscopy. , 248(4951), 73–76. doi:10.1126/science.2321027.

[34]   Mérian, Juliette; Gravier, Julien; Navarro, Fabrice; Texier, Isabelle (2012). Fluorescent Nanoprobes Dedicated to in Vivo Imaging: From Preclinical Validations to Clinical Translation. Molecules, 17(12), 5564–5591. doi:10.3390/molecules17055564.

[35]   K. König (2000). Multiphoton microscopy in life sciences., 200(2), 83–104. doi:10.1046/j.1365-2818.2000.00738.x.

[36]   https://www.setabiomedicals.com/2-photon-microscopy.html.

[37]   Stoltzfus, Caleb R.; Barnett, Lauren M.; Drobizhev, Mikhail; Wicks, Geoffrey; Mikhaylov, Alexander; Hughes, Thomas E.; Rebane, Aleksander (2015). Two-photon directed evolution of green fluorescent proteins. Scientific Reports, 5(1), 11968–. doi:10.1038/srep11968.

[38]   Kobayashi, Hisataka; Ogawa, Mikako; Alford, Raphael; Choyke, Peter L.; Urano, Yasuteru (2010). New Strategies for Fluorescent Probe Design in Medical Diagnostic Imaging., 110(5), 2620–2640. doi:10.1021/cr900263j.

[39]   https://www.olympus-lifescience.com/en/technology/museum/micro/2004/.

[40]   https : / / www . thermofisher . com / it / en / home / life-science / cell-culture / cell-culture-learning-center / cell-culture-resource-library / cell-culture-transfection-application-notes/neurobiology-transfection-guide.html.

[41]   Dietrich, Christof P.; Steude, Anja; Schubert, Marcel; Ohmer, Jürgen; Fischer, Utz; Höfling, Sven; Gather, Malte C. (2016). Strong Coupling in Fully Tunable Microcavities Filled with Biologically Produced Fluorescent Proteins. Advanced Optical Materials, (), –. doi:10.1002/adom.201600659.